Measurements of hard x-ray emission from runaway electrons in DIII-D

2012 Nucl. Fusion 52 013007

(http://iopscience.iop.org/0029-5515/52/1/013007)

IOP Publishing and International Atomic Energy Agency Nuclear Fusion
Nucl. Fusion **52** (2012) 013007 (13pp) doi:10.1088/0029-5515/52/1/013007

Measurements of hard x-ray emission from runaway electrons in DIII-D

A.N. James[1,a,b], M.E. Austin[2], N.Commaux[3], N.W. Eidietis[4], T.E. Evans[4], E.M. Hollmann[1], D.A. Humphreys[4], A.W. Hyatt[4], V.A. Izzo[1], T.C. Jernigan[3], R.J. La Haye[4], P.B. Parks[4], E.J. Strait[4], G.R. Tynan[1], J.C. Wesley[4] and J.H. Yu[1]

[1] Center for Energy Research at UC San Diego, 9500 Gilman Dr., La Jolla, CA 92093-0417, USA
[2] The University of Texas at Austin, 1 University Station, Austin, TX 78712, USA
[3] Oak Ridge National Laboratory, PO Box 2008, Oak Ridge, TN 37831, USA
[4] General Atomics, PO Box 85608, San Diego, CA 92186-5608, USA

E-mail: jamesan@fusion.gat.com

Received 29 July 2011, accepted for publication 10 November 2011
Published 5 December 2011
Online at stacks.iop.org/NF/52/013007

Abstract
The spatial distribution of runaway electron (RE) strikes to the wall during argon pellet-initiated rapid shutdown of diverted and limited plasma shapes in DIII-D is studied using a new array of hard x-ray (HXR) scintillators. Two plasma configurations were investigated: an elongated diverted H-mode and a low-elongation limited L-mode. HXR emission from MeV level REs generated during the argon pellet injection is observed during the thermal quench (TQ) in diverted discharges from REs lost into the divertor. In limiter discharges, this prompt TQ loss is reduced, suggesting improved TQ confinement of REs in this configuration. During the plateau phase when the plasma current is carried by REs, toroidally symmetric HXR emission from remaining confined REs is seen. Transient HXR bursts during this RE current plateau suggest the presence of a small level of wall losses due to the presence of an unidentified instability. Eventually, an abrupt final loss of the remaining RE current occurs. This final loss HXR emission shows a strong toroidal peaking and a consistent spatiotemporal evolution that suggests the development of a kink instability.

(Some figures may appear in colour only in the online journal)

1. Introduction

Disruptions remain one of the outstanding problems for future burning plasma experiments [1], since the larger stored energy in those machines can be deposited at hazardous rates on plasma-facing structures through thermal loads [2], halo current forces and runaway electrons (REs). Fortunately, rapid-shutdown techniques such as injection of high-Z material can mitigate some of these effects, but these techniques have limited success in preventing RE generation [3] and can even result in enhanced RE generation [4]. By injecting impurities such as argon or neon as gas [5, 6] or frozen pellets [7, 8], thermal energy is harmlessly radiated away resulting in a reproducibly brief (a few hundred microseconds in DIII-D) thermal quench (TQ). Due to the increased resistivity of the cold plasma, a current quench (CQ) occurs on a rapid timescale (a few milliseconds in DIII-D) which helps reduce electromagnetic forces associated with halo currents during vertical displacement events (VDEs) [9]. Efforts continue [10] to solve the remaining problem: that these shutdowns occasionally result in conversion of more than 30% of initial plasma current into high energy (>10 MeV) RE current, which can persist for hundreds of milliseconds in what is termed the 'plateau phase'. The final abrupt termination of this RE current can then damage first wall surfaces [11, 12].

In this paper we discuss experimental results from a new hard x-ray (HXR) sensing bismuth germanate ($Bi_4Ge_4O_{12}$, aka BGO) scintillator array [13] and corresponding analysis exploring RE in shutdowns using argon killer pellets. A 'prompt loss' phase is identified when HXRs from multi-MeV (1–3 MeV) REs are first observed in the time between the TQ and CQ. The prompt HXR emission arrives shortly (<0.5 ms) after argon pellet injection, so REs are clearly experiencing large loop voltages even before the global current decay begins, demonstrating that RE seed formation is not confined to the CQ

[a] Current affiliation: Lawrence Livermore National Laboratory, Livermore, CA 94551, USA.
[b] Currently on assignment: Princeton Plasma Physics Laboratory, Princeton, NJ 08540, USA.

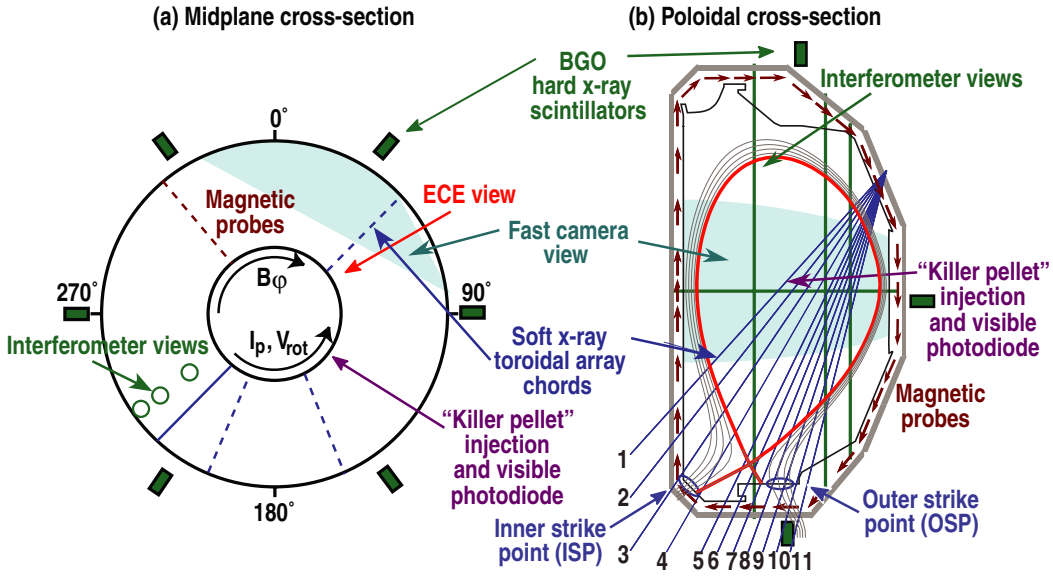

Figure 1. Diagnostic and hardware arrangement for the discussed experiments.

phase. In diverted discharges, the prompt loss of REs is found to be localized to the divertor strike points, consistent with NIMROD modelling which suggests loss due to magnetically stochastic regions from post-TQ MHD. In limiter discharges, the prompt x-ray emission associated with RE deconfinement is reduced compared with the diverted configuration, also consistent with NIMROD modelling which indicates reduced post-TQ MHD in limiter target plasmas. During the RE plateau after the CQ, a steady toroidally symmetric HXR emission is observed which continues even after the last closed flux surface (LCFS) separates from the wall. Also during the plateau in some shots, intermittent toroidally symmetric HXR bursts coincident with bursts on magnetic probes suggest an instability, as yet unidentified. All RE plateaus terminate abruptly with a clear toroidal peaking of HXR emission. In some shots the final loss has a clear VDE precursor, while in other shots there is no clear precursor and the plateau terminates on the centerpost at the midplane.

The rest of the paper is arranged as follows. Section 2 describes the experimental method, and the two distinct plasma configurations (limited and diverted) which were used. Direct experimental findings are described in section 3. In section 4, these findings are further explored through discussion and analysis of observations and simulations. Section 4.1 explains limitations of diagnostics during the TQ phase. Sections 4.2, 4.3 and 4.4 discuss phenomena observed during the prompt loss, RE plateau and final termination phases respectively. NIMROD modelling is discussed in section 4.5. Section 4.6 presents a brief discussion of RE energy and loop voltages. Some simple formulations for bremsstrahlung emission from REs are described in the appendix.

2. Experimental method

These experiments begin by injecting a 2.7 mm × 2.7 mm cylindrical argon 'killer pellet' into a stable plasma, a technique first reported elsewhere [4] and previously shown [14] to generate more REs than other rapid-shutdown techniques. Data discussed in this paper were collected over two years of experiments on six separate days, and represent results from one-hundred and twenty-eight successful argon killer pellet shutdowns.

The layout of diagnostics used for interpreting these rapid-shutdown experiments is shown in figure 1. Plasma position and loop voltages are inferred from magnetic probe measurements. Electron density is measured by a two-colour heterodyne interferometer system [15]. Electron temperature is measured by an electron cyclotron band radiometer [16]. A camera sensitive to visible wavelengths observes synchrotron emission from runaways [17]. An array of photodiodes viewing the plasma and divertor through beryllium filters measures soft x-ray (SXR) emission [18]. HXR emission is measured by an array of bismuth germanate (BGO) scintillators [13]. Six scintillators are distributed in a toroidal array around the vessel midplane, and three scintillators are distributed in three poloidal arrays which are equally spaced toroidally.

Two different plasma configurations were studied: a diverted, elongated ($\kappa = 1.7$), neutral beam heated, H-mode discharge; and a limited, lower elongation ($\kappa = 1.3$), electron cyclotron heated, L-mode discharge. Low-elongation shapes were used because they were previously observed [19] to result in greater and more frequent RE currents. Substantial RE current plateaus occurred more frequently in the limiter configuration, as shown in figure 2.

The average pre-shutdown core temperature $T_e \sim 2.3$ keV was similar in both cases, but ranged from 1 to 3.5 keV. In the diverted configuration, the pre-shutdown line-averaged density tends to be larger at $n_e \sim 1.7 \times 10^{14}$ cm^{-3} compared with $n_e \sim 6 \times 10^{13}$ cm^{-3} for the limiter configuration. The edge safety factor $q_{95} \sim 3.3$ was similar in both cases, but ranged from 3.1 to 5. In most of the diverted shutdowns, beam heating continued roughly 10 ms into the shutdown, while in all limiter shutdowns, gyrotron heating was turned off a few ms before the shutdown. Also similar in both cases are the apparent TQ timescale $\tau_{TQ} \sim$ 200–300 μs found by

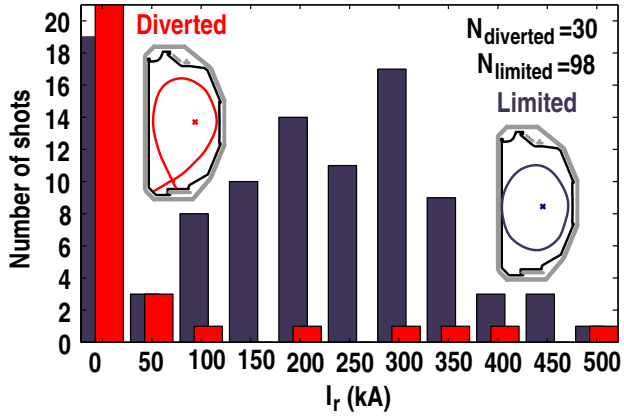

Figure 2. A histogram of plateau phase runaway current plotted for the two different experimental shapes showing increased frequency of runaway plateau for the limiter shape.

fitting an error function $T(t) = T_0[\mathrm{erf}(-t/\tau_{TQ}) + 1]/2$ to the broadband electron cyclotron emission (ECE) signal during TQ, and the CQ timescale $\tau_{CQ} \sim$ 3–4 ms found by fitting an exponential decay $I(t) = I_0 \exp(-t/\tau_{CQ})$ to the current measured during CQ. Also in both cases, RE signatures appear only after inducing a rapid shutdown and not after occasional unintentional disruptions, indicating that REs are generated as a consequence of the shutdown and are not remnant startup runaways.

3. Experimental findings

Figure 3 shows an example diverted discharge exhibiting a runaway plateau broken down chronologically from left to right into phases referenced throughout this paper: TQ and prompt generation, prompt loss, CQ and avalanche, runaway plateau and final termination. Figures 3(*a*)–(*d*) illustrate long timescale quantities of the plateau while figures 3(*e*)–(*g*) highlight observations of fast phenomena before the CQ, all of which are described below. Similarities and differences between shutdowns of the diverted and limiter configurations will be discussed.

Once the CQ begins, the total measured plasma region current I_p decays, producing a loop voltage that induces wall currents I_w and accelerates RE current I_r, examples of which are shown in figure 3(*a*). When a runaway plateau does not occur, the thermal plasma current follows an exponential decay $I_{L/R} = I_0 \exp(-t/\tau_{CQ})$ from the point of fastest current decay, where $\tau_{CQ} = L/R$ corresponds to the plasma inductive timescale. Following prior calculations [4], RE current I_r is calculated by subtracting this model for decaying thermal current from the total measured current. Previous work [20] suggests that this RE plateau current is formed by an avalanche phenomena that amplifies a small pre-existing RE seed current.

Figure 3(*b*) shows the average RE energy inferred from a set of scintillators equipped with incrementally thicker lead shielding, sensitive to RE energies in the range 0.5 MeV$\lesssim W_r \lesssim$ 20 MeV [13], and the RE energy inferred from visible synchrotron emission observed on a fast camera, sensitive only to runaways with energy sufficient to generate visible synchrotron emission $W_r \gtrsim$ 30 MeV [21]. These two energy diagnostics, therefore, observe two separate bands of the

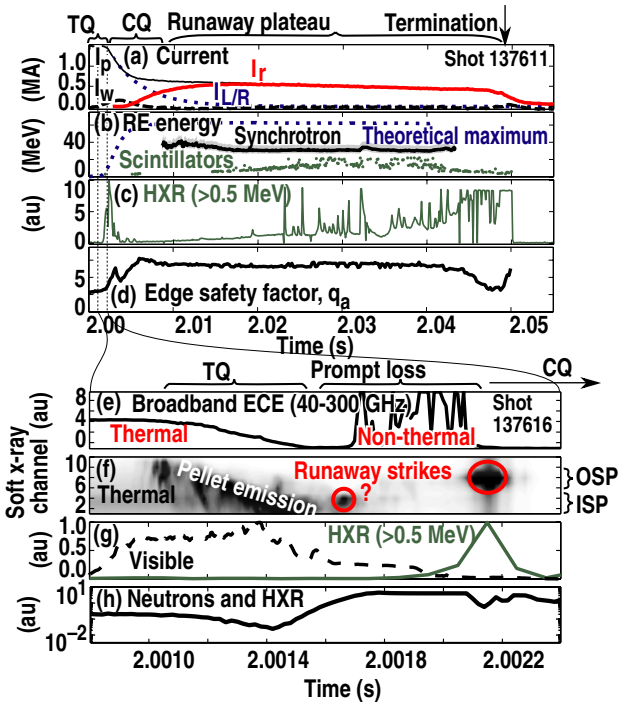

Figure 3. Overview data of typical observations during the TQ, CQ and runaway plateau phases including (*a*) total measured plasma region current I_p (thin line), wall current I_w (dashed), inductive decay model current $I_{L/R}$ (dotted), and plateau phase runaway current I_r (solid), (*b*) runaway energy measured with scintillators (dots), visible synchrotron emission [17, 21] (solid), and a theoretical maximum (dotted), (*c*) HXR emission measured by a midplane detector at 90° toroidal, and (*d*) the edge safety factor [22] calculated by JFIT. An expansion of the TQ is shown to detail fast response of the following: (*e*) broadband cyclotron emission, (*f*) SXR emission with inner and outer divertor strike points labelled (ISP and OSP, respectively), (*g*) visible line radiation from the pellet (dashed) and HXR emission (solid), and (*h*) signals on a neutron counting plastic scintillator which is also sensitive to HXRs. Features of interest are highlighted from two separate shots for the entire disruption and TQ phase, respectively, with temporal phases indicated along the top of each section.

runaway energy spectrum, and neither covers the entire range of possible energies. The two inferred energies are both below the theoretical maximum runaway energy which will be discussed in section 4.6.

Figure 3(*c*) shows a time history of the HXR ($W_\gamma \gtrsim$ 0.5 MeV) intensity recorded in a scintillator shielded with 4 mm of lead foil located near the midplane. The detector shows brief HXR emission before and during the CQ (referred to as the 'prompt loss'), followed by a lower intensity continuous emission with intermittent bursts (referred to as the 'RE plateau'), and ends with another brief intense emission during the plateau termination (referred to as 'final loss'). These three phases will be described further in the discussion.

Figure 3(*d*) shows the edge safety factor, which features a drop that occurs over the last few milliseconds before final termination. The edge safety factor is calculated from the integral $q_a = \oint \mathrm{d}\theta r B_T / R B_p$ [22] along the boundary from JFIT reconstructions [23].

High time resolution observations of RE generation and deconfinement between the TQ and CQ are shown in figures 3(*e*)–(*g*). During this period, total plasma current

remains roughly constant (i.e. $\mathrm{d}I/\mathrm{d}t = \mathrm{d}/\mathrm{d}t[\int j(\psi)\mathrm{d}\psi] \sim 0$) while it re-organizes (i.e. $\mathrm{d}/\mathrm{d}t[j(\psi)] \neq 0$) for a duration of about 1 ms from the beginning of the TQ.

Initial signals until 2.001 s on a broadband microwave radiometer shown in figure 3(*e*) correspond to thermal electron cyclotron radiation which decays during 2.001–2.0016 s as the pellet radiates away thermal energy. Bursts of microwave emission during 2.0017–2.0021 s occur after the TQ which could be either associated with broadband emission from non-thermal electrons [24], from x-band emission associated with filamentation of relativistic electron beams propagating in dense plasmas [25], or some other emission process. The broadband radiometer is used because it includes third harmonic thermal ECE which is robust against cutoff due to re-absorption by the plasma, a topic discussed further in section 4.1.

Observations from SXR sensing photodiode arrays which view chords through the plasma core and divertor are shown in figure 3(*f*). These arrays observe emission associated with bremsstrahlung from the hot core thermal emission until 2.001 s, followed by line radiation as the pellet streaks through and cools the plasma during 2.001–2.0016 s. Brief emission from isolated chords occurs later at 2.00165 and 2.00215 s, and is associated with bremsstrahlung from RE impact at the divertor inner and outer strike points, referred to as 'prompt loss'. A previous publication suggested that the earlier brief emission may occur instead as a result of argon line radiation excited by runaways in the core [3]. The SXR data are ambiguous about where emission originates along the chord view, but the prompt-loss emission always occurs brightest in chords viewing the divertor strike points. Also, the observed HXR intensity at 2.00215 s coincident with the outer strike point SXR emission could only occur from RE striking a thick target, as discussed in the appendix.

In figure 3(*g*), a photodiode sensitive to visible wavelengths of light from the plasma observes strong emission from argon pellet interaction with the cool boundary plasma beginning at 2.0005 s, before the pellet reaches the core and line radiation is first seen by the SXR array. Also shown in figure 3(*g*) is a signal from a HXR scintillator located outside the vessel near the divertor which observes emission coincident with the peak in outer strike point SXR emission at roughly 2.00215 s, as noted above. No HXR burst occurs coincident with the inner strike point SXR emission. The time of the peak HXR intensity measured by detectors below the divertor and peak outer strike point SXR intensity are shown to coincide in figure 4, which is consistent with the broad energy spectrum of bremsstrahlung emission from RE striking the divertor [13]. Of the 30 successful shutdowns of the diverted configuration, this transiently peaked HXR emission coincides with outer strike point SXR emission in 23 shots (including all shots with RE plateaus), while no HXR emission occurred in the remaining seven shutdowns. The energy sensing scintillators located at the midplane on opposite sides of the vessel infer an average RE kinetic energy of $W_\mathrm{k} = 1$–3 MeV during these prompt-loss events, which occur prior to the onset of the CQ phase.

Figure 3(*h*) shows signals from a neutron counting scintillator, which is also sensitive to HXRs. Observed HXRs must have an energy in the range $\gtrsim$ 0.5 MeV to penetrate

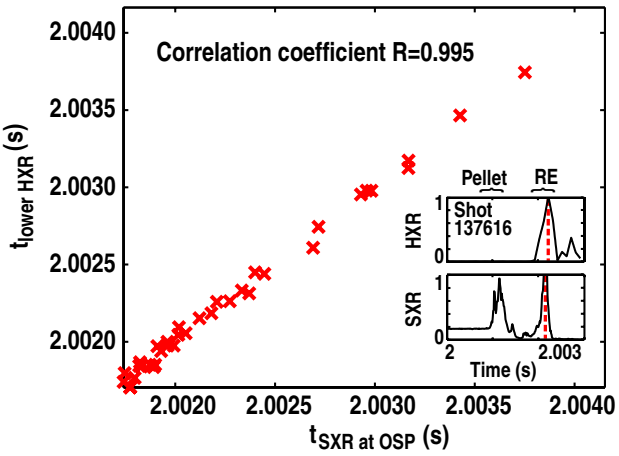

Figure 4. Correlation of times recorded for prompt HXR bursts in detectors on the bottom of the machine and SXR bursts in chords viewing the outer strike point. The inlay shows HXR and SXR time traces during prompt loss for one example shot.

the vacuum vessel. During the TQ, the neutron production rate drops on the TQ timescale, roughly following the broadband ECE. Compared with the lower gain photodiodes used on the BGO scintillators, the high gain photomultiplier on this scintillator can also see much lower intensity HXR emission. As a result of this higher sensitivity, this signal rises beginning at 2.0014 s before the TQ has completed, suggesting that some small amount of high energy RE may already exist even before the plasma has cooled completely, though this is not seen on any other diagnostics. In some shots, the signal abruptly drops after the prompt burst is completed and an exponential increase in the signal is observed for a few milliseconds until the detector saturates again. This suggests an exponential increase of RE-induced HXR emission consistent with avalanche multiplication of the RE population.

4. Discussion and analysis

4.1. Limitations of TQ measurements

Extreme conditions during the TQ phase require additional considerations for appropriate interpretation of many diagnostic measurements. In particular, electron density measurements using the interferometer system and electron temperature measurement using ECE are discussed in this section.

ECE can be reflected by the plasma and effectively cutoff when the right handed x-mode nth harmonic cutoff frequency [26] exceeds the cyclotron frequency of interest: $f_\mathrm{r} = [f_\mathrm{ce} + (f_\mathrm{ce}^2 + 4f_\mathrm{pe}^2)^{1/2}]/2 \geqslant nf_\mathrm{ce}$ where the electron plasma frequency is $f_\mathrm{pe} = \sqrt{n_\mathrm{e}e^2/m_\mathrm{e}\varepsilon_0}/2\pi = 28\,\mathrm{GHz}\,\sqrt{n_\mathrm{e}/10^{13}\,\mathrm{cm}^{-3}}$ and the electron cyclotron frequency is $f_\mathrm{ce} = eB/2\pi m_\mathrm{e} = 56\,\mathrm{GHz}\,(B/2T)$. This cutoff condition can be re-arranged to express a density limit for cutoff of the nth harmonic ECE: $n_\mathrm{e} \leqslant (n^2-n)\varepsilon_0 B^2/m_\mathrm{e} = (n^2-n)3.9\times10^{13}\,\mathrm{cm}^{-3}(B/2\,T)^2$, which is indicated in figures 5(*b*) and (*e*). To avoid this cutoff, ECE systems are typically designed to use the second harmonic ECE which is more robust against such cutoff, but even the second harmonic 110 GHz ECE can be cutoff where the

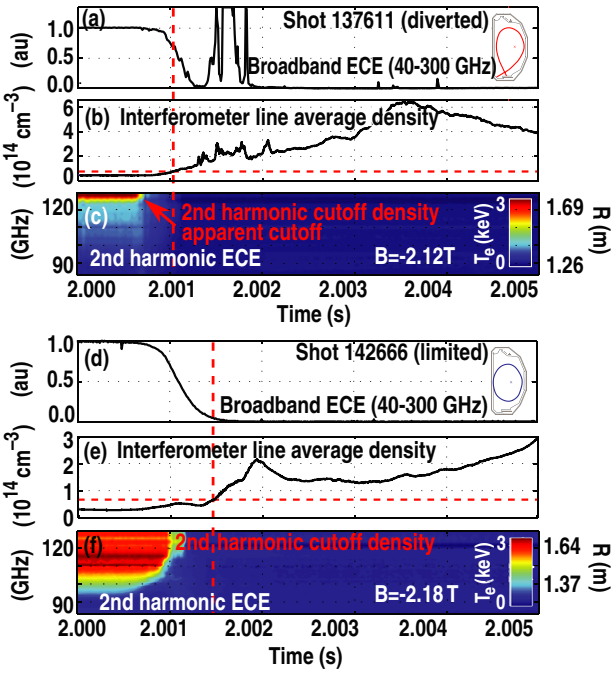

Figure 5. Broadband ECE, total line-averaged density, and second harmonic ECE shown for (*a*)–(*c*) diverted and (*d*)–(*f*) limiter configurations. The ECE cutoff density and time is indicated for both shapes with dashed lines.

density increases beyond $7.8 \times 10^{13}\,\mathrm{cm}^{-3}$. A density of over $2.3 \times 10^{14}\,\mathrm{cm}^{-3}$ is necessary for cutoff of the third harmonic ECE viewed by the broadband ECE diagnostic data shown in figure 5; as discussed below such densities typically occur late compared with the TQ.

The line-averaged electron density can be measured by a two colour interferometer, but there are some complications during disruptions which must be corrected including variation of the effective path length as the plasma moves, and correction of fringe skips when the lasers refract too much in the strong density gradients. Dividing the sum of line-integrated density along the four interferometer paths by the total path length inside the LCFS then provides a density measurement that is more nearly a volume-averaged quantity: $n_{\mathrm{avg}} = \sum \int n_{\mathrm{e}} \mathrm{d}l / \sum \int \mathrm{d}l$, where the summation is over the four paths. In the diverted configuration, the line-averaged density measured this way is near the ECE cutoff value before shutdown, and crosses the cutoff value roughly 400 μs after the TQ begins. In the limiter configuration, the initial line-averaged density is lower, and crosses the cutoff value roughly 1 ms after the TQ begins.

In diverted shutdowns (figures 5(*a*)–(*c*)), the second harmonic ECE is abruptly cutoff at 2.0007 s (figure 5(*c*)), which occurs roughly 300μs before the line-average density exceeds the right handed cutoff, suggesting that a localized peaking of the density occurs during the TQ. No cutoff is apparent in limiter shutdowns (figures 5(*d*)–(*f*)), where a cooling wave is seen advancing on the TQ timescale (figure 5(*f*)), though similar localized peaking of density is likely. Again, in both plasma configurations, the plasma appears to remain mostly transparent to third harmonic ECE which is viewed by the broadband ECE diagnostic. The neutron production rate is also roughly proportional to temperature in a hot plasma, and the TQ timescale inferred from the drop in neutron production roughly matches that inferred from the broadband ECE diagnostic.

It is important to remember that if the local density anywhere exceeds the cutoff threshold, partial cutoff will occur, resulting in an apparent local cooling rate which is faster than reality. For example, a plasma with a high density annulus surrounding a hot core could emit much less cyclotron radiation than an equivalently hot plasma with no high density annulus. Our fast interferometer based density measurements are not spatially resolved so such a scenario cannot be ruled out. Despite these considerations, the ECE and neutron production data are consistent with a rapid ($\leqslant$500 μs) collapse of the plasma electron temperature due to the injected argon impurities.

4.2. *Prompt-loss phenomena*

The evidence shown in figure 3 of RE generation occurring *before* the CQ (hence referred to as 'prompt' runaway generation) implies that some voltage source must exist before the CQ which then accelerates REs up to the apparent MeV energies. We conjecture that even though the CQ begins around 1 ms after completion of the volume-averaged TQ (as seen by the broadband ECE diagnostic in figure 3(*e*)), a substantial loop voltage must still exist before CQ due to the resistivity spike associated with TQ. Due to the likely presence of large magnetically stochastic regions during and after TQ, hyper-resistivity [27] may enhance the resistivity beyond the classical Spitzer resistivity. Further discussion of the range of possible accelerating voltages is deferred to section 4.6.

When RE seed current is deconfined and strikes the vessel walls during the prompt loss, it generates bremsstrahlung x-rays, as shown previously in figures 3(*f*) and (*g*). Since the deconfined runaway seed current is linearly proportional to x-ray emission [28] as discussed in the appendix, the x-ray emission integrated over the prompt-loss phase can be used as a qualitative proxy for the amount of deconfined REs during the prompt-loss phase. In figure 6(*a*), a histogram of the integrated prompt HXR burst from REs as observed by the lower detectors is shown for both the diverted and limiter configurations separately. This x-ray emission is nearly an order of magnitude larger on average in the diverted configuration than in the limiter configuration, suggesting that a greater quantity of REs are lost during prompt loss in diverted shutdowns than in limiter shutdowns. In the diverted configuration, substantial prompt-loss bursts are seen even when no RE plateau occurs, as shown in figure 6(*b*); for diverted discharges where a RE plateau does occur, the prompt-loss intensity is roughly proportional to the plateau RE current. In the limiter discharge configuration by comparison, the prompt-loss burst is often small even when a large RE plateau occurs, consistent with improved RE confinement during the prompt-loss phase. It is important to note that the present experiments do not separate the effects of elongation and the location or existence of a divertor x-point or limiter contact point on these transport phenomena, any of which on their own might cause the observed changes in confinement. Differences in confinement between the two configurations are further discussed in section 4.5.

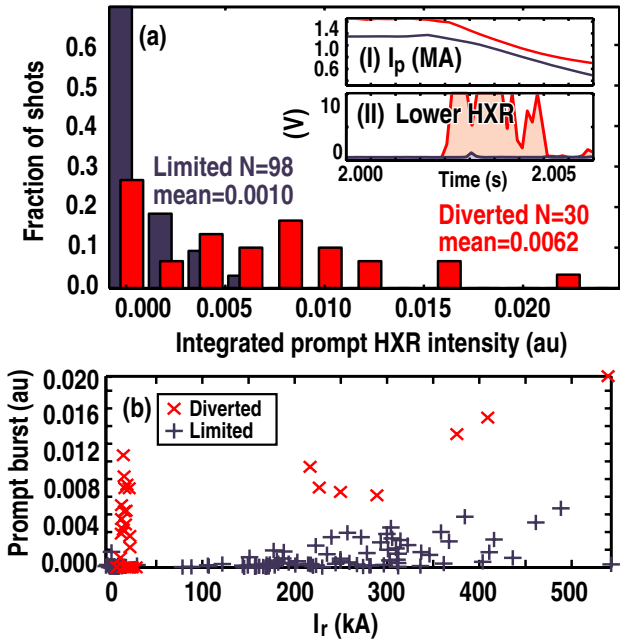

Figure 6. (*a*) A histogram illustrating that the average intensity of the time-integrated prompt-loss HXR burst is greater in diverted experiments compared with limiter experiments. An inlay shows the respective time histories of (I) current and (II) HXR emission in lower detectors in two example discharges. Also shown are (*b*) the time-integrated prompt bursts plotted against the RE plateau current magnitude.

4.3. Plateau phenomena

Beginning with the RE plateau, there is a steady x-ray emission which is observed on both the external HXR scintillators shown in figure 3(*c*), and all SXR arrays. This emission is believed to result from a combination of bremsstrahlung from RE scattering off of in-plasma impurities and a small number of RE steadily striking the wall due to a scrape-off on the limiter or a slow diffusive transport of RE out to the wall. Bremsstrahlung from both in-plasma impurities and wall losses appear to have comparable intensity, as discussed in the appendix. This long duration steady HXR emission is toroidally symmetric and illuminates only the midplane detectors, as shown in figure 7(*b*) at $t = 2.0081$ s and $t = 2.0272$ s. The illumination of only midplane detectors is consistent with forward beaming of x-ray emission at a narrow angle of $1/\gamma \sim 10^\circ$ for $W_r = 10$ MeV RE moving primarily in the toroidal direction, since midplane detectors lie at roughly zero angle with respect to the toroidal direction but upper and lower detectors would lie at an angle of roughly 90°.

Efforts in some limiter configuration shots to move the RE current away from the inboard wall limiting point resulted in no abrupt decrease of HXR emission when the LCFS separated from the limiter as shown in figure 8. After the Shafranov shift vanishes following the TQ, the current channel of every RE plateau contracts in major radius as seen during the time period 2–2.015 s and becomes limited on the inboard wall near the midplane. Efforts to move RE away from the inboard wall actually begin moving the current centroid out again around 2.03 s, and the inner gap between the LCFS and inboard wall becomes finite at around 2.1 s. The absence of a drop in HXR emission when the LCFS separates from the wall suggests that scrape-off of REs does not substantially occur at the limiting point. As discussed in section 4.4, there are indications that REs exist outside of the LCFS. Observed HXRs are believed to result from a combination of bremsstrahlung from gradual loss (i.e. diffusion or other transport) of RE to the outboard wall and RE scattering off of argon impurities within the plasma, as discussed in the appendix.

Gamma spectroscopy was performed after these experiments on the three outer midplane graphite limiters at toroidal locations of 95°, 230° and 310° [29]. This analysis identified the presence of beryllium-7 in the limiter tiles, similar to analysis performed at the C-Mod tokamak [30]. Beryllium-7 can be produced through photoactivation of carbon-12 by photons with energy of at least 26 MeV, which would be generated by bremsstrahlung from RE impacting the limiters. The finding that beryllium-7 is only found near the outer midplane limiters (circled in blue in figure 8), and not at other locations, suggests that REs primarily impact the outer midplane limiters, consistent with drift orbit losses [31].

At least one substantial HXR burst occurs during most runaway plateaus; sometimes several are observed, as shown in figure 9(*b*). These x-ray bursts are toroidally symmetric as shown in unsaturated upper detectors in figure 7 at $t = 2.0272$, and are believed to result from a small amount of RE being deconfined and striking the wall. Since no drop in I_r is observed coincident with the bursts, the amount of lost RE current must be below the ∼1 kA noise level of the current measurement. Poloidally localized spikes of change in the poloidal magnetic field occur simultaneous with the larger HXR bursts, as shown in figure 9(*d*, II). Similar x-ray and magnetic bursts were seen in prior JT-60U experiments [32, 33]. The bursts likely occur as a result of some yet unidentified instability of the RE equilibrium; brief analysis is shown below which rules out several possible non-terminating instability mechanisms which could result in rapid loss of RE.

These runaway plateau discharges appear to be stable against filamentation. In a relativistic ($\beta = v/c \sim 1$) electron beam with small return current I_{return} and hence incomplete current neutralization $f_M = I_{return}/I_r \ll 1$, and low density n_r propagating in plasma of relatively high density such that $n_e \gg n_r$, filamentation instability occurs when [34]

$$\frac{\omega_{pb}^2}{\omega_{cb}^2} \Big/ \left[1 + 2\frac{\omega_{pb}^2}{\omega_{cb}^2}(1 - f_M)\right] > 1, \qquad (1)$$

where the beam plasma frequency is $\omega_{pb} = (e^2 n_b/\epsilon_0 m_e \gamma)^{1/2}$ and the beam cyclotron frequency is $\omega_{cb} = eB_0/m_e\gamma$. The return current can be any neutralizing current flowing against the main RE current channel. For a top-hat profile runaway beam, the runaway density n_r or runaway current density j_r as a function of runaway current I_r and minor radius a is $n_r = j_r/ec = I_r/ec\pi a^2 = 3.3 \times 10^{11}\,\mathrm{cm}^{-3}\,(I_r/500\,\mathrm{kA})\,(10\,\mathrm{cm\,a}^{-1})^2$. The ratio of the beam plasma and beam cyclotron frequency then becomes

$$\frac{\omega_{pb}}{\omega_{cb}} = \sqrt{\frac{I_r W_r}{\epsilon_0 e c^3 \pi a^2 B_0^2}} = 0.41\sqrt{\frac{I_r}{500\,\mathrm{kA}}\frac{W_r}{10\,\mathrm{MeV}}}\frac{10\,\mathrm{cm}}{a}\frac{2\,\mathrm{T}}{B_0}, \qquad (2)$$

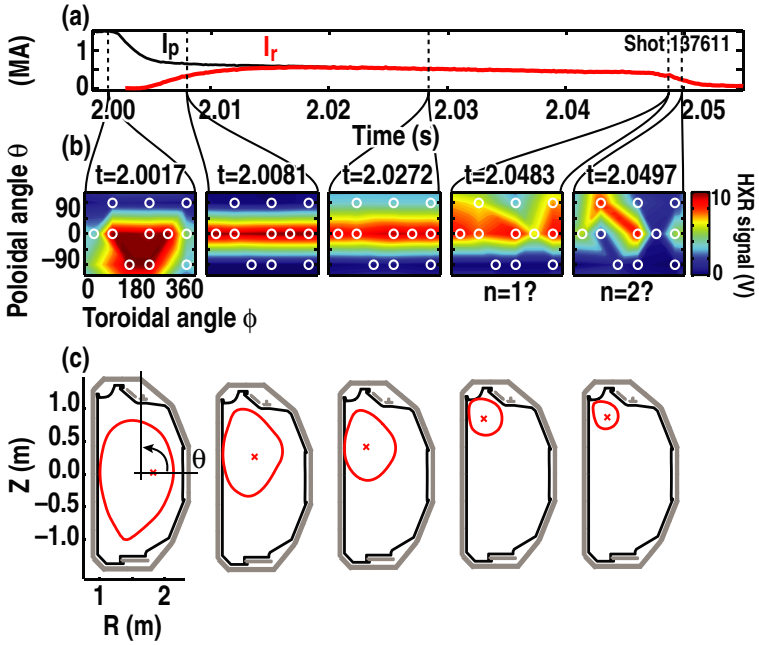

Figure 7. (*a*) Total current I_p (thin black) and runaway current (thick red), (*b*) spatial HXR emission profiles with detector locations circled, and (*c*) plasma position from JFIT magnetic reconstructions. Panels are shown for the prompt-loss phase ($t = 2.0017$ s), the steady ($t = 2.0081$ s) and bursty ($t = 2.0272$ s) emission during the plateau phase, and the kink-like termination phase with apparent toroidal mode numbers labelled ($t = 2.004\,83$ s and $t = 2.004\,97$ s). Amplifiers are saturated at 10 V. The same discharge as figure 3 is shown.

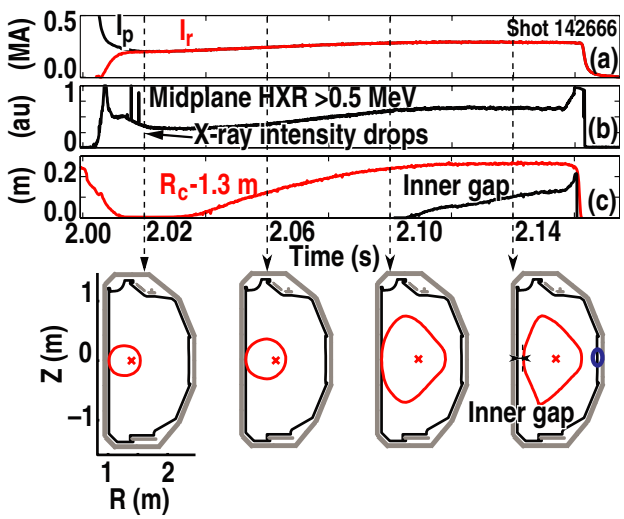

Figure 8. Plasma motion in a shot where RE current was moved off of the limiter, showing (*a*) total plasma current I_p (thin black) and runaway current I_r (thick red), (*b*) HXR emission, (*c*) the current centroid major radius R_c (thick red) and the inner gap size between the LCFS and limiter (thin black). In the cross-section plots, the current centroid is marked by an 'X'. The blue circle in the bottom right panel marks the location of peak limiter activation.

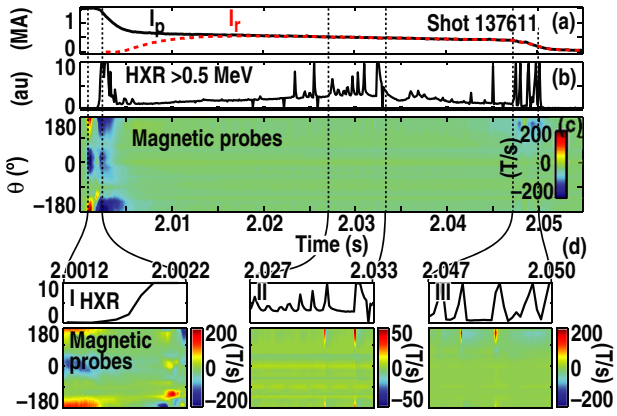

Figure 9. (*a*) Plasma current (thin black) and runaway current (thick red) shown with (*b*) HXR emission and (*c*) signals on differential magnetic probes which occur coincident with HXR bursts. Expanded time plots of HXR and magnetic probe data are shown during the (I) prompt phase, (II) plateau phase, and (III) final termination. The contour plots represent $\mathrm{d}B_p/\mathrm{d}t$ versus time and poloidal angle.

where typical runaway plateau phase values have been substituted as shown above. Hence even a current neutralized top-hat runaway beam should be marginally stable against filamentation. While peaking of the current profile (i.e. increase of ℓ_i) associated with ramp-down [35] or runaway energies higher than assumed could slightly destabilize filamentation, the low degree of current neutralization f_M in real RE beams strongly stabilizes filamentation.

RE plateaus are stable against growth of magneto-sonic whistler waves [36] as long as $n_r/n_e < Z^2 B_T/20T_{ev}^{3/2}$. In the post-TQ RE plateau where $Z_{eff} \sim 1$, $B = 2\,\mathrm{T}$, $T \sim 1.5\,\mathrm{eV}$ and $n_e \sim 5 \times 10^{14}\,\mathrm{cm}^{-3}$, these waves are then stable because $n_r/n_e \sim 0.0007 < Z^2 B_T/20T_{ev}^{3/2} = 0.05$. The above stability criterion describes collisional stability of magneto-sonic whistler waves, which are additionally stabilized by convection as described elsewhere [37].

RE plateaus are also stable against the fan instability [38] whenever E_D/E is large, as during RE plateaus. The low temperature during RE plateau makes the condition for the fan instability: $E_D/4E + \sqrt{(Z_{eff}+1)E_D/E} \leqslant ln\,\Lambda$ unsatisfiable.

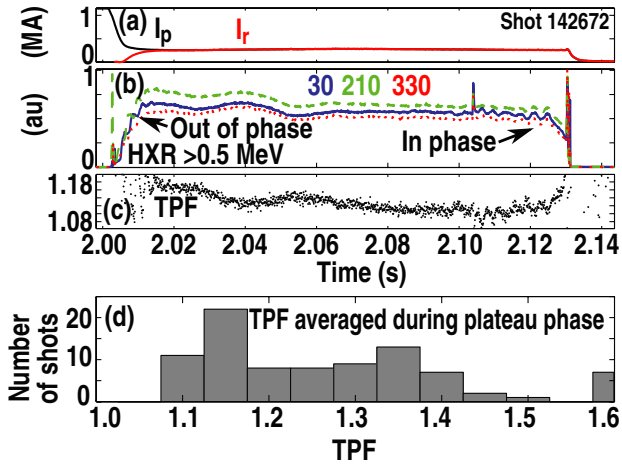

Figure 10. (*a*) Total measured current (thin black) and runaway current (thick red), (*b*) HXR signals on midplane scintillators at three toroidal locations: 30 (solid blue), 210 (dashed green) and 330 (dotted red), (*c*) the TPF for these scintillators and (*d*) a histogram of the plateau phase TPF for all plateaus.

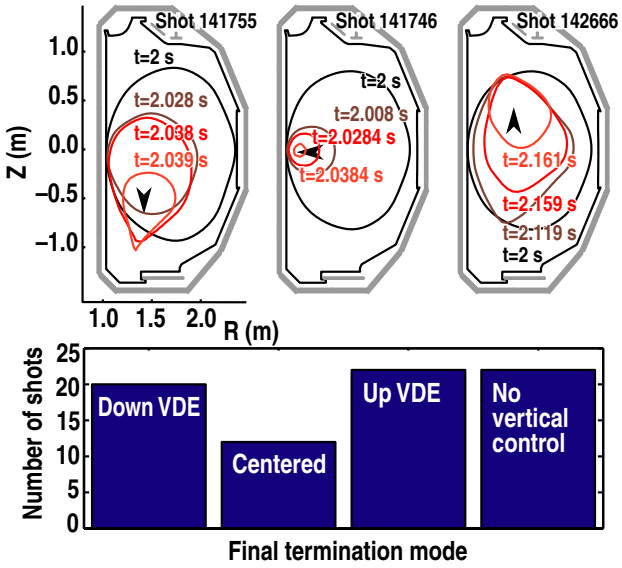

Figure 11. Final termination mode for RE plateaus.

Further investigation of MHD stability of the RE equilibrium [39] is necessary to identify the causative instability associated with the burst of HXR emission.

A fast camera primarily observes visible wavelength synchrotron emission [40] during RE plateau, but also sees signatures of these bursty instabilities. HXR bursts are seen on the camera image due to scintillations which occur in the fibre bundle. The camera also observes internal instabilities appearing as rapid rearrangement of RE synchrotron emission inside the LCFS; however, these internal dynamics do not appear to coincide with scintillations. Taken together, these observations suggest that these plateau phase HXR bursts may result from instabilities localized to the edge region where the camera cannot see the small quantities of RE.

An important parameter for future machines is the degree of localization for energy deposited by REs onto vessel surfaces. We have quantified this issue by defining a toroidal peaking factor (TPF) for the midplane toroidal array of scintillators, which is defined as the ratio of the maximum HXR signal P_{hxr} to the mean value $\bar{P}_{\mathrm{hxr}}$: $TPF = \max(P_{\mathrm{hxr}})/\bar{P}_{\mathrm{hxr}}$. Due to high intensity HXR emission during the plateau phase, only a reduced set of three scintillators in the midplane toroidal array equipped with attenuating neutral density filters was unsaturated in most discharges. This reduced set of detectors reveals that HXR emission during the plateau phase is typically quite toroidally symmetric during the brief bursts discussed above and during continuous emission, except for some oscillations, as shown in figures 7(*c*) and 10. Occasionally, out of phase fluctuations are observed, as seen in figure 10(*c*) until 2.015 s, which suggest the presence of a slowly rotating toroidally asymmetric mode during the growth of the RE current, consistent with the early $n = 1$ mode discussed previously [41]. In-phase fluctuations sometimes occur up to 20 ms before termination, suggesting the presence of a toroidally symmetric mode, as shown beginning around 2.1 s in figure 10(*b*). These observations of HXR toroidal symmetry and asymmetry during the plateau phase are shown in figure 10(*c*). The TPF averaged throughout the plateau phase for all plateaus is typically below 1.5, as shown in figure 10(*d*).

In several shots, the suppression of existing RE current by additional impurity injection was studied [42]. This impurity injection resulted in an increase of plateau phase toroidal peaking to roughly two for a brief period after the impurity injection, which caused the six anomalously high plateau TPFs in figure 10(*d*). After this brief transient increase, HXR emission decreased by more than a factor of ten and toroidal symmetry resumed.

4.4. Termination phenomena

All RE plateaus terminate abruptly after remaining confined for up to several hundred milliseconds, as shown in figure 3 just after $t = 2.05$ s, due to either vertical instability or another instability, similar to reported termination behaviour in JT-60U [33, 43]. A histogram of the apparent final plateau instability types in limiter configuration discharges is shown in figure 11, with columns for each of four termination modes: downward VDE, centred radial termination, upward VDE, and control system error which resulted in slow vertical drift. The RE plateau VDE motion occurs on a timescale similar to that predicted previously [44]: $\tau_{\mathrm{VDE}} = \tau_{\mathrm{CQ}}\tau_{\mathrm{w}}/(\tau_{\mathrm{CQ}}+\tau_{\mathrm{w}}) \sim 2.1$ ms where in DIII-D $\tau_{\mathrm{CQ}} \sim 3.7$ ms and the wall time for the up–down antisymmetric mode ($m = 1, n = 0$) is $\tau_{\mathrm{w}} \sim 5$ ms.

All diverted configuration experiments and some early limiter configuration experiments drifted slowly upwards due to issues with the control system which were solved before the majority of limiter configuration experiments were performed [45], so figure 11 reflects only limiter configuration experiments where the control system was functioning properly.

Many plateaus terminate immediately following a considerable drop in the edge safety factor, as shown in figure 3(*d*), suggesting that the corresponding destabilization of a kink instability may ultimately cause the termination. The edge safety factor is calculated from reconstructions constrained only by external magnetic diagnostics, which other authors have reported [46] to be a valid inference. Sufficient REs are present up to 16 cm outside of the LCFS to disintegrate

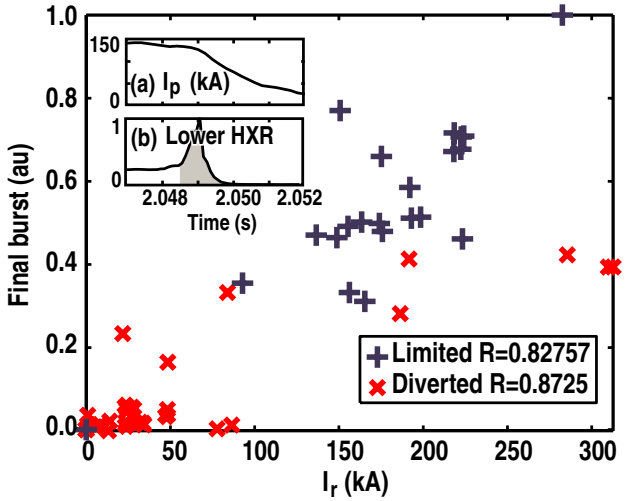

Figure 12. Integrated final HXR bursts in lower detectors plotted against final measured RE current for terminations at the top of the vessel, as discussed in the text.

injected probe pellets [47]; however, the RE density there is unknown. This observation suggests that while the LCFS remains a well-defined magnetic surface, it may not define a good boundary for RE confinement as assumed for thermal plasmas and the edge safety factor may lose meaning in this case.

Toroidally asymmetric HXR emission occurs during the final termination as shown in figures 7(*d*) and (*e*). These toroidal asymmetries are consistent with the occurrence of kink modes being destabilized as q drops. With the poloidal arrangement of only three scintillation detectors, poloidal mode numbers are not resolvable, while the midplane toroidal arrangement of five detectors cannot resolve modes higher than $n = 2$.

The time-integrated HXR emission during the final termination is used to verify that HXR intensity is proportional to the deconfined RE current. For this check, only shots which terminated at the top of the machine and only HXR emission measured by the lower detectors are used to avoid detector saturation from the strong forward beaming of emitted x-rays. HXR signals selected and integrated in this way correlate roughly with I_r measured just before termination in shutdowns of both divertor and limiter configurations as shown in figure 12, with correlation coefficients of $R = 0.87$ and $R = 0.83$, respectively.

For discharges with only a small amount of RE generated, a repeatable temporal sequence of HXR signals during the final loss occurs in the midplane toroidal array of detectors. This sequence was observed in 17 of 25 shutdowns before neutral density filters were installed to reduce detector saturation. In such shutdowns, a low intensity signal slowly increases for roughly 1 ms on opposite sides of the machine (always detectors at 90° and 270°), followed by 2–10 ms of abrupt increase to intense HXR emission which saturates the entire toroidal array, after which x-ray emission decays in all detectors over roughly 1 ms and is peaked at 210°. One example shot exhibiting this sequence is shown in figure 13.

The TPF and variability of location, duration and intensity of HXR emission during the final loss are all

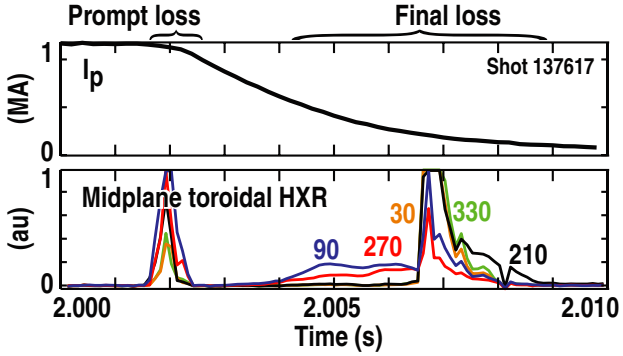

Figure 13. Midplane toroidal array of HXR scintillators showing a consistent final loss sequence of toroidal asymmetry, with detector toroidal locations marked in degrees.

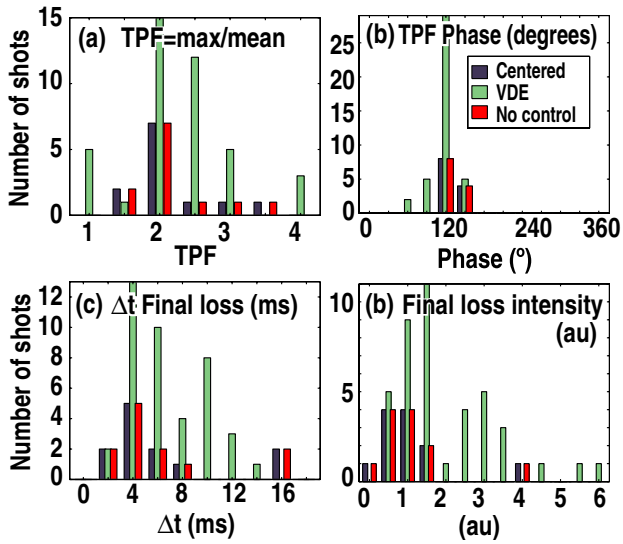

Figure 14. A histogram of (*a*) the TPF averaged during late loss HXR emission, (*b*) the phase of the peak, (*c*) the duration of final loss and (*d*) the integrated intensity of final loss.

presented in histograms in figure 14, again only for limiter configuration experiments where the control system was functioning properly.

To establish a TPF without saturated detectors during the final loss phase of plateau discharges, the TPF is calculated as described earlier, and then is averaged during periods of the termination phase HXR emission when no detector in the array is saturated. The resulting TPF most often has a value of roughly two, though in some shots it can reach values of four, larger in either case than in the TPF during the plateau phase shown earlier in figure 10. While this HXR TPF is the best measure available on DIII-D of localization of deposited RE energy, it is again important to recall that any x-ray scattering in the vessel walls can broaden the x-ray footprint so that even a point impact of runaways might produce a spatially broad excitation of x-ray detectors, and also that the toroidal arrangement of only five scintillators could entirely miss a narrow x-ray footprint. Thus, the peaking factor shown here represents a lower limit due to these effects, and RE energy deposition in DIII-D may actually be localized to several small strike points as occurs in other experiments [48–50].

The toroidal angle of the maximum observed x-ray intensity during the same period the TPF is calculated is roughly 120°, with a small spread. This apparent existence of a persistent toroidal peaking location is consistent with infrared camera observations at JET [48], which reveal persistent localized RE strike points from shot to shot. The persistent peaking location may result from intrinsic non-axisymmetric error fields or possibly non-axisymmetry of the limiting surfaces with respect to the toroidal field which could cause a repeatable mode locking location in the machine.

The time duration of final loss HXR emission (shown in figure 14(*c*)) varied from 2–14 ms for VDEs, which is a much longer time period than the VDE timescale $\tau_{\mathrm{VDE}} \sim 2.1$ ms discussed earlier. This suggests that even though the VDE occurs rapidly, HXR emission persists because REs do not all immediately strike the vessel wall, or new REs may be generated by the rapid current drop at the end of plateau. By comparison, the duration of final loss x-ray emission in centred radial terminations and discharges with poor vertical control was shorter than the duration for emission in VDE terminations, though still longer than the VDE timescale.

Considered in only arbitrary units, the time-integrated final loss HXR intensity (shown in figure 14(*d*)) varied by only a factor of two for most discharges with either centred radial instability or poor vertical control, while it varies by up to a factor of six for VDE terminations. The increased variation of intensity for VDE terminations could result from RE avalanche during the final rapid current drop, consistent with the longer duration x-ray emission in these discharges as discussed above.

4.5. NIMROD modelling

Recent results [41, 51] from the MHD code NIMROD are consistent with several of the experimental findings discussed above. While timing of MHD events during shutdowns with NIMROD is difficult to interpret because impurity deposition is assumed uniform, the peak of magnetically stochastic activity is believed to correspond with the prompt loss observed experimentally. In these simulations, an increased overlap of magnetic islands occurs following the TQ in the diverted case compared with the limiter case, with isolated islands in each case. This results in an increased cross-sectional area of stochastic magnetic fields in the diverted case, as compared with the limiter case and as shown in figure 15. Confinement of RE in these islands is consistent with the twisted RE snakes observed in TEXTOR [52]. Runaways generated in stochastic regions are rapidly transported outside of the plasma boundary to impact the divertor or limiting surface, hence this results in decreased RE confinement in the diverted case during the prompt-loss phase.

The strike points obtained by following test particle drift orbits in the NIMROD simulations, shown as a green 'X' in figure 15, are consistent with the localized SXR emission observed after the TQ along the floor for diverted shutdowns (figure 3(*f*)), and the observed absence of SXR emission along the floor for limiter shutdowns. The prompt strike is predicted by NIMROD to be toroidally symmetric for the diverted configuration; however, there appears to be some asymmetry in experimental HXR emissions, as shown in figure 7(*a*). Loop voltages predicted by NIMROD would accelerate negatively

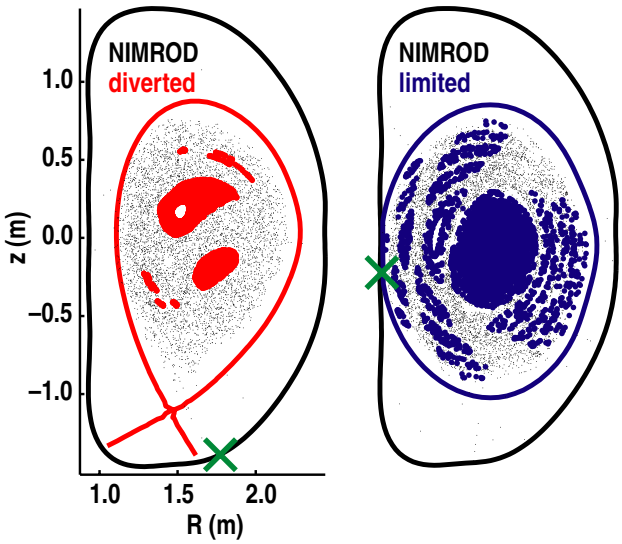

Figure 15. Experimental shapes with Poincaré plots generated by NIMROD showing closed surfaces (red and blue) and stochastic field regions (black dots) at the peak of stochasticity during a disruption. Green X's on the limiting boundary mark strike points for RE deconfined through stochastic regions.

charged particles (i.e. electrons) to the outer strike point in diverted configurations, and no REs are predicted to impact the inner strike point. However, there is often a SXR burst seen localized to the inner strike point as shown in figure 3(*f*). For the limiter configuration, NIMROD predicts that a rotating $n = 1$ mode causes most prompt losses [41] at the limiting point, consistent with the apparent rotating mode seen in figure 10 until 2.015 s.

4.6. RE energy and loop voltages

As described elsewhere [53], RE kinetic energy is limited primarily by synchrotron radiation except when high density high-Z impurity content results in bremsstrahlung emission limiting the power balance. In the analysis below, bremsstrahlung and RE perpendicular energy are therefore neglected to calculate the synchrotron energy limit, since only a small amount of high-Z impurities are injected for the shutdown. This limit is the solution to an ordinary differential equation balancing radiated synchrotron power with kinetic energy gain from the loop voltage: $\mathrm{d}W_k/\mathrm{d}t = e(V_{\mathrm{loop}}/2\pi R)\beta c - P_{\mathrm{syn}}$, with the initial kinetic energy defined by Dreicer's critical energy for runaway $W_{\mathrm{Dr}} = n_{\mathrm{e}}e^3 \ln\Lambda/4\pi\epsilon_0^2 E$, which has the value of a few hundred eV before the CQ begins. The radiated synchrotron power is $P_{\mathrm{syn}} = 2/3 a_0 \alpha^2 \gamma^4 (1 - 1/\gamma^2)^2 m_{\mathrm{e}} c^3/R^2$, where a_0 is the classical electron radius, α is the fine structure constant, γ and β are the relativistic parameters, and R is the gyro-averaged radius of curvature. To calculate an upper bound for the energy limit, gyromotion is neglected and the radius of curvature is here assumed the largest it could be: the tokamak major radius. Once generated, runaways rapidly accelerate towards this energy limit W_{k}, shown in figure 3(*b*), calculated with the loop voltage $V_{\mathrm{loop}} = -L\mathrm{d}I/\mathrm{d}t$ where the inductance $L = 2\mu H$ is assumed constant. While the RE energy distribution is limited from above by synchrotron emission,

the most probable RE energy is determined by collisions, as described elsewhere [54].

Conversely, the average RE energy of ~3 MeV measured roughly 1 ms after the first x-ray line emission from the pellet can be used to calculate a minimum bound for the accelerating voltage between the beginning of TQ and this measurement 1 ms later. Neglecting synchrotron emission and assuming a stationary position at the machine centre $R = 1.67\,\mathrm{m}$ and a constant rate of energy gain $\mathrm{d}W_\mathrm{k}/\mathrm{d}t = 3\,\mathrm{MeV}/1\,\mathrm{ms} = eV_\mathrm{loop}c/2\pi R$, the effective loop voltage must be at least $V_\mathrm{loop} = 2\pi R(\mathrm{d}W_\mathrm{k}/\mathrm{d}t)/ec \sim 100\,\mathrm{V}$. The actual voltage must be larger since REs start at a velocity $v \ll c$ and synchrotron emission and other drag forces will reduce the energy gain. If any REs have energies larger than the measured average, as would occur from the broad RE energy distribution predicted by avalanche theory [55]), then again the actual voltage must be even larger. The possible existence of transient loop voltage spikes in the range of 1000 V which last for roughly 1 ms following the TQ is inferred by taking the time derivative of poloidal flux at the magnetic axis using either EFIT or JFIT reconstructions constrained only by fast magnetic diagnostics, though the validity of such techniques has not been verified. Modelling done by other groups [56, 57] predicted loop voltages of $V \sim 500\,\mathrm{V}$ which resulted in substantial RE generation via the Dreicer mechanism [58], though more recent work [59] also includes the hot-tail mechanism [60] with similar results. The origins of the seed REs formed during the TQ phase are important since they may form the precursor to the large amplitude RE current in the plateau phase. Additional work is necessary to reduce uncertainties and narrow the range of possible loop voltage magnitudes described above.

5. Conclusions

Hard x-ray measurements of RE and related analysis during the various phases of argon pellet induced rapid shutdowns of DIII-D were reported. Energetic (MeV level) seed REs were observed between the TQ and CQ phases indicating the existence of a RE forming mechanism between the TQ and CQ phases. Predictions of loop voltages during this phase were shown to range over a factor of ten. Seed REs were seen to be at least partially deconfined during the TQ into the divertor strike points in diverted discharges. Deconfinement was found to be reduced in low-elongation limited L-mode shapes, suggesting improved confinement of REs following TQ in these discharges, consistent with NIMROD simulations. Limiter discharges also showed a higher probability of forming a plateau current than diverted discharges. During RE plateaus, a steady hard x-ray emission was shown, believed to result from RE scattering with heavy impurities in the plasma. Later in RE plateaus, several brief hard x-ray bursts were often observed coincident with spikes on magnetic probes which suggest a small level of RE wall losses due to the action of an unidentified instability during this phase of the discharge. RE plateaus remained confined for up to several hundred milliseconds but always terminated in an abrupt final loss. Hard x-ray bursts during this final loss often show a strong toroidal peaking which occurs following a drop in the edge safety factor, suggesting that a kink type instability terminates the plateau discharge.

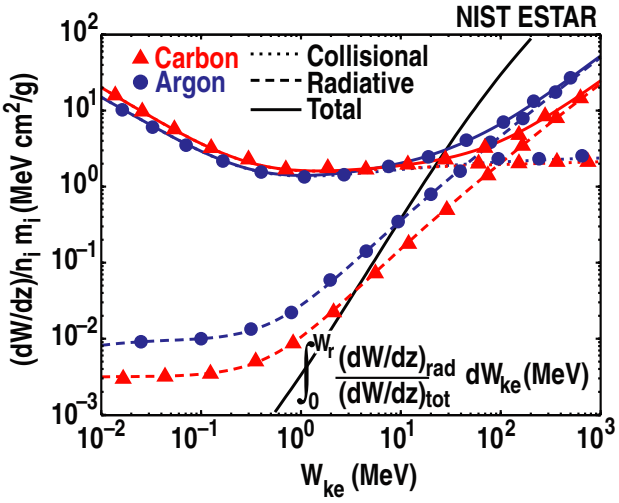

Figure A.1. A comparison of electron stopping powers (i.e. drag forces $F_\mathrm{d} = \mathrm{d}W/\mathrm{d}z$) normalized by mass density for carbon and argon as tabulated in the NIST ESTAR database [67]. The integral in equation (A.2) versus W_r is also shown for reference.

Acknowledgments

This work was supported by the US Department of Energy under DE-FG02-07ER54917, DE-FG02-07ER54912, DE-FG03-97ER54415, DE-AC05-00OR22725 and DE-FC02-04ER54698. The authors would like to acknowledge outstanding support and numerous contributions from the DIII-D team which enabled these experiments, and especially contributions of N. Antoniuk, R.A. Moyer, and J.A. Boedo for assistance troubleshooting experimental hardware.

Appendix. Bremsstrahlung from runaways

REs are diagnosed in part by the x-ray continuum emitted when they impact plasma ions and impurities, and first wall materials. This bremsstrahlung emission from scattering of high energy electrons off of atomic nuclei and electrons has been thoroughly investigated by several authors [61–65], and is the topic of at least one textbook [66].

For a simple comparison of the total x-ray energy radiated by a single electron with kinetic energy W_r through collisions with a target thin compared with the stopping distance $\Delta z \ll W/(\mathrm{d}W/\mathrm{d}z)$ such as the background plasma, and an electron-opaque thick target $\Delta z > W/(\mathrm{d}W/\mathrm{d}z)$ such as the solid vessel walls, use of the following suffices

$$E_\mathrm{thin} = (\mathrm{d}W/\mathrm{d}z)_\mathrm{rad}\Delta z, \tag{A.1}$$

$$E_\mathrm{thick} = \int_0^{W_\mathrm{r}} \frac{(\mathrm{d}W/\mathrm{d}z)_\mathrm{rad}}{(\mathrm{d}W/\mathrm{d}z)_\mathrm{tot}}\mathrm{d}W_\mathrm{ke}. \tag{A.2}$$

The radiative and total stopping powers normalized to mass density are shown for argon and carbon in figure A.1 for reference.

Since the number of RE in a current I_r is $N_\mathrm{r} = 2\pi R I_\mathrm{r}/ec$, the corresponding power emitted by a confined RE current of $I_\mathrm{r} = 100\,\mathrm{kA}$ with assumed mono-energetic energy $W_\mathrm{k} = 10\,\mathrm{MeV}$ in an argon background of density $n_\mathrm{Ar} = 10^{14}\,\mathrm{cm}^{-3}$,

and by a RE current of $\Delta I_r = 1\,\mathrm{kA}$ lost in a time interval $\tau_{loss} = 10\mu s$ to the graphite wall tiles are, respectively,

$$P_{thin} = (dW/dz)_{rad} c\beta N_r \sim 250\,\mathrm{kW}\frac{n_{Ar}}{10^{14}\,\mathrm{cm}^{-3}}\frac{I_r}{100\,\mathrm{kA}}, \quad (A.3)$$

$$P_{thick} = \int_0^{W_r}\frac{(dW/dz)_{rad}}{(dW/dz)_{tot}}dW_{ke}\Delta N_r/\tau_{loss} \sim 1.4\,\mathrm{MW}\frac{\Delta I_r}{1\,\mathrm{kA}}\frac{10\,\mu s}{\tau_{loss}}. \quad (A.4)$$

Such x-ray radiation is not emitted isotropically, but is preferentially beamed along the direction of the RE momentum with a characteristic angle of $1/\gamma = m_e c^2/(m_e c^2 + W_k) \sim 1/5 \sim 10^\circ$.

While these analyses are a bit oversimplified, they can still be used for several simple interpretations of x-ray observations. A slow RE loss to vessel surfaces of the order seen during RE plateau decay $dI_r/dt \sim 1\,\mathrm{kA\,ms}^{-1}$ will produce roughly 13 kW, substantially less x-ray power than $I_r = 100\,\mathrm{kA}$ of confined RE current in a thin argon plasma, hence HXR emission during the RE plateau is likely dominated by plasma emission as opposed to wall emission. Also, deconfinement of only $\Delta I_r = 1\,\mathrm{kA}$ can easily overwhelm thin target emission if it is lost on short enough timescales. Since emitted x-ray power is a linear function of RE current, it may also be possible to infer the amount of RE current from x-ray emissions if the other quantities are known.

References

[1] Hender T.C. *et al* 2007 Progress in the ITER Physics Basis Chapter 3: MHD Stability, Operational Limits and Disruptions *Nucl. Fusion* **47** S128–S202 (beginning of chapter)
[2] Janos A. *et al* 1993 *Proc. 14th Int. Conf. on Plasma Physics and Controlled Nuclear Fusion Reseach 1992 (Wuerzburg, Germany 1992)* vol 1 (Vienna: IAEA) p 527 http://www.osti.gov/bridge/product.biblio.jsp?osti_id=6869365
[3] Hollmann E.M. *et al* 2005 *Nucl. Fusion* **45** 1046
[4] Evans T.E. *et al* 1998 *Proc. 17th Int. Conf. on Fusion Energy (Yokohama, Japan 1998)* (Vienna: IAEA) CD-ROM file [EXP3/07] and http://www.osti.gov/energycitations/product.biblio.jsp?osti_id=319809
[5] Whyte D.J. *et al* 2003 *J. Nucl. Mater.* **313–316** 1239
[6] Bakhtiari M. *et al* 2005 *Nucl. Fusion* **45** 318
[7] Lengyel L.L., Büchl K., Pautasso G., Ledl L., Ushakov A.A., Kalvin S. and Veres G. 1999 *Nucl. Fusion* **39** 791
[8] Kawano Y. *et al* 2005 *J. Plasma Fusion Res.* **81** 593
[9] Eidietis N.W. and Humphreys D.A. 2010 *Proc. 23rd Int. Conf. on Fusion Energy (Daejeon, South Korea, 2010)* (Vienna: IAEA) CD-ROM file [EXS/P2-05] and http://www-pub.iaea.org/MTCD/Meetings/cn180_papers.asp
[10] Commaux N. *et al* 2010 Novel rapid shutdown strategies for runaway electron suppression in DIII-D *Proc. 23rd IAEA Fusion Energy Conf. (Daejeon, Republic of Korea)* paper CN-180/EXS/P2-02 http://www-pub.iaea.org/MTCD/Meetings/cn180_papers.asp
[11] Bartels H.W. 1994 *Fusion Eng. Des.* **23** 323
[12] Nygren R., Lutz T., Walsh D., Martin G., Chatelier M., Loarer T. and Guilhem D. 1997 *J. Nucl. Mater.* **241–243** 522
[13] James A.N., Hollmann E.M. and Tynan G.R. 2010 *Rev. Sci. Instrum.* **81** 10E306
[14] Hollmann E.M. *et al* 2010 *Phys. Plasmas* **17** 056117
[15] Zeeland M.A., Boivin R.L., Carlstrom T.N., Deterly T. and Finkenthal D.K. 2006 *Rev. Sci. Instrum.* **77** 10F325
[16] Austin M.E. and Lohr J. 2003 *Rev. Sci. Instrum.* **74** 1457
[17] Shi Y., Fu J., Li J., Yang Y., Wang F., Li Y., Zhang W., Wan B. and Chen Z. 2010 *Rev. Sci. Instrum.* **81** 033506
[18] Snider R.T., Evanko R. and Haskovec J. 1988 *Rev. Sci. Instrum.* **59** 1807
[19] Granetz R.S., Whyte D.G. and Izzo V.A. 2009 *Bull. Am. Phys. Soc.* **54** 231
[20] Rosenbluth M. and Putvinski S. 1997 *Nucl. Fusion* **37** 1355
[21] Jaspers R,. Cardozo N.J.L., Donne A.J.H., Widdershoven H.L.M. and Finken K.H. 2001 *Rev. Sci. Instrum.* **72** 466
[22] Freidberg J. 1987 *Ideal Magnetohydrodynamics* (New York: Plenum)
[23] Humphreys D.A. and Kellman A.G. 1999 *Phys. Plasmas* **6** 2742
[24] Knoepfel H. and Spong D. 1979 *Nucl. Fusion* **19** 785
[25] Kapetanakos C.A. 1974 *Appl. Phys. Lett.* **25** 484
[26] Lohr J. 1988 *Rev. Sci. Insrum.* **59** 1608
[27] Berk H.L., Fowler T.K., LoDestro L.L. and Pearlstein L.D. 2001 Lawrence Livermore National Laboratory *Internal Report UCRL-ID-142741* https://e-reports-ext.llnl.gov/pdf/240360.pdf
[28] Lamoureux M., Waller P., Charles P. and Avdonina N.B. 2000 *Phys. Rev.* E **62** 4091
[29] Taylor P.L. 2010 General Atomics private communication
[30] Borrás M.C., Fiore C.L., Wenzel K.W. and Takase Y. 1995 *Rev. Sci. Instrum.* **66** 942
[31] Entrop I. 1999 Confinement of relativistic runaway electrons in tokamak plasmas *PhD Thesis* Technische Universiteit Eindhoven
[32] Yoshino R., Tokuda S. and Kawano Y. 1999 *Nucl. Fusion* **39** 151
[33] Tamai H. 2002 *Nucl. Fusion* **42** 290
[34] Davidson R.C., Hui B.H. and Kapetanakos C.A. 1975 *Phys. Fluids* **18** 1040
[35] Jackson G.L., Casper T.A., Luce T.C., Humphreys D.A., Ferron J.R., Hyatt A.J., Leuer J.A., Petrie T.W., Turco F. and West W.P. 2009 *Nucl. Fusion* **49** 115027
[36] Fülop T., Pokol G., Helander P. and Lisak M. 2006 *Phys. Plasmas.* **13** 062506
[37] Fülop T., Smith H.M. and Pokol G. 2009 *Phys. Plasmas* **16** 022502
[38] Parail V.V. and Pogutse O.P. 1986 Runaway electrons in a tokamak *Rev. Plasma Phys.* vol 11, ed M.A. Leontovich (New York: Consultants Bureau) http://adsabs.harvard.edu/abs/1986RvPP...11.....L
[39] Yoshida Z. 1989 *Phys. Fluids* B **1** 1702
[40] Jaspers R. 1995 Relativistic runaway electrons in tokamak plasmas *PhD Thesis* Technische Universiteit Eindhoven
[41] Izzo V.A. *et al* 2011 *Nucl. Fusion* **51** 063032
[42] Hollmann E.M. *et al* 2011 Effect of applied toroidal electric field on the growth/decay of plateau-phase runaway electron currents in DIII-D *Nucl. Fusion* **51** 103026
[43] Yoshino R. and Tokuda S. 2000 *Nucl. Fusion* **40** 1293
[44] Putvinski S., Barabaschi P., Fujisawa N., Putvinskaya N., Rosenbluth M.N. and Wesley J. 1997 *Plasma Phys. Control. Fusion* **39** B157
[45] Commaux N. *et al* 2011 Novel rapid shutdown strategies for runaway electron suppression in DIII D *Nucl. Fusion* **51** 103001
[46] Pustovitov V.D. 2001 *Nucl. Fusion* **41** 721
[47] James A.N. *et al* 2011 *J. Nucl. Mater.* **415** S849–51
[48] Arnoux G. *et al* 2011 *J. Nucl. Mater.* **415** S817–20
[49] Martin G. *et al* 2004 *Proc. 20th Int. Conf. on Fusion Energy (Vilamoura, Portugal 2004)* (Vienna: IAEA) CD-ROM file [EX/10-6Rc] and http://www-naweb.iaea.org/napc/physics/fec/fec2004/datasets/EX_10-6Rc.html
[50] Lipa M., Martin G., Mitteau R., Basiuk V., Chatelier M., Cordier J.J. and Nygren R. 2003 *Fusion Eng. Des.* **66–68** 365

[51] Izzo V.A. *et al* 2010 *(Proc. 23rd Int. Conf. on Fusion Energy (Daejeon, South Korea, 2010)* (Vienna: IAEA) CD-ROM [THS/9-2] and http://www-pub.iaea.org/MTCD/Meetings/cn180_papers.asp
[52] Jaspers R., Cardozo N.J.L., Finken K.H., Schokker B.C., Mank G., Fuchs G. and Schuller F.C. 1994 *Phys. Rev. Lett.* **72** 4093
[53] Bakhtiari M., Kramer G.J. and Whyte D.G. 2005 *Phys. Plasmas* **12** 102503
[54] Papp G., Drevlak M., Fülop T. and Helander P. 2011 *Nucl. Fusion* **51** 043004
[55] Jayakumar R., Fleischmann H.H. and Zweben S.J. 1993 *Phys. Lett. A* **172** 447
[56] Helander P. *et al* 2004 *Proc. 20th Int. Conf. on Fusion Energy (Vilamoura, Portugal, 2004)* (Vienna: IAEA) CD-ROM file [TH/P4-39] and http://www-naweb.iaea.org/napc/physics/fec/fec2004/datasets/TH_P4-39.html
[57] Eriksson L.G., Helander P., Andersson F., Anderson D. and Lisak M. 2004 *Phys. Rev. Lett.* **92** 205004
[58] Dreicer H. 1959 *Phys. Rev.* **115** 238
[59] Fehér T., Smith H.M., Fülöp T. and Gál K. 2011 *Plasma Phys. Control. Fusion* **53** 035014
[60] Smith H.M. and Verwichte E. 2008 *Phys. Plasmas* **15** 072502
[61] Kramers H.A. 1923 *Phil. Mag.* **46** 836
[62] Bethe H. and Heitler W. 1934 *Proc. R. Soc. Lond.* **146** 83
[63] Nakel W. 1994 *Phys. Rep.* **243** 317
[64] Korol A.V., Obolensky O.I., Solov'yov A.V. and Solovjev I.A. 2001 *J. Phys. B: At. Mol. Opt. Phys.* **34** 1589
[65] Lamoureux M. and Charles P. 2006 *Radiat. Phys. Chem.* **75** 1220
[66] Dyson N. 1973 *X-Rays in Atomic and Nuclear Physics* (London: Longman Group Limited)
[67] Berger M., Coursey J., Zucker M. and Chang J. 2005 ESTAR, PSTAR and ASTAR: Computer Programs for Calculating Stopping-Power and Range Tables for Electrons, Protons and Helium Ions (version1.2.3) *EM NISTIR 4999* (National Institute of Standards and Technology) http://physics.nist.gov/Star